Deciphering the origin of high electrochemical performance in a novel ti-substituted p2/o3 biphasic cathode for sodium-ion batteries

Bei Hu, Fushan Geng, Chong Zhao, Bertrand Doumert, Julien Trebosc, Olivier Lafon, Chao Li, Ming Shen, Bingwen Hu

Deciphering the Origin of High Electrochemical Performance in a Novel Ti-substituted P2/O3 Biphasic Cathode for Sodium-Ion Batteries

*Bei Hu,[a] Fushan Geng,[a] Chong Zhao,[a] Bertrand Doumert,[b,d] Julien Trébosc,[b,d] Olivier Lafon,[b,c] Chao Li, *[a] Ming Shen, *[a] and Bingwen Hu [a]*

[a] Shanghai Key Laboratory of Magnetic Resonance, State Key Laboratory of Precision Spectroscopy, School of Physics and Electronic Science, East China Normal University, Shanghai 200062, P.R. China.

[b] Univ. Lille, CNRS, Centrale Lille, Univ. Artois, UMR 8181, UCCS – Unité de Catalyse et de Chimie du Solide, F-59000 Lille, France.

[c] Institut Universitaire de France.

[d] Univ. Lille, CNRS-2638, Fédération Chevreul, F-59000 Lille, France.

KEYWORDS： P2/O3-type cathode material, Ti-substitution, oxygen redox, Mn charge compensation, structure stability.

ABSTRACT ： The layered Mn-based oxides (Na_xMnO_2), which is one of the most promising cathode families for rechargeable sodium-ion batteries (SIBs), have received considerable attention due to their tunable electrochemical performances and low costs. Herein, a novel P2/O3 intergrown Li-containing $Na_{0.8}Li_{0.27}Mn_{0.68}Ti_{0.05}O_2$ cathode

material prepared by Ti-substitution into Mn-site is reported. Benefiting from the synergistic effects of biphasic composite structure and inactive d^0 element substitution, this P2/O3 electrode exhibits high initial charge/discharge capacity and excellent cycling performance. The combination of different characterization techniques including solid-state NMR, EPR, XAS, and HRTEM gives insights into the local electronic environment, the redox chemistry, and also the microstructure rigidity of these cathode materials upon cycling. On the basis of comprehensive comparison with the Ti-free P2/O3-$Na_{0.8}Li_{0.27}Mn_{0.73}O_2$, the observed improvement on the electrochemical performance is primarily attributed to the mitigation of notorious Mn^{3+}/Mn^{4+} redox and the enhanced stability of oxygen charge compensation behavior. From the viewpoint of structure evolution, Ti-substitution restrains the Li^+ loss and irreversible structural degradation during cycling. This study provides an in-depth understanding of the electronic and crystal structure evolutions after inactive d^0 element substitution and may sheds light on the rational design of high-performance P2/O3 biphasic Mn-based layered cathodes.

1. INTRODUCTION

Rechargeable sodium-ion batteries (SIBs), as an emerging category of electrochemical energy storage device, are advantageous over currently commercial lithium-ion batteries (LIBs) due to the use of abundant, geographically dispersed, and inexpensive Na resource.[1,2] However, the energy density and durability of SIBs are still

significantly lower than those of LIBs, owing notably to the scarcity of suitable Na-based cathode materials. Recently, a wide variety of Na-ion host cathodes have been developed toward high energy density and long cycle lifespan.[3-6] Among them, layered sodium oxides Na_xTMO_2 (TM = transition metal) with high theoretical capacities have aroused extensive interests over recent years. These layered oxides share similar structural characteristics with TMO_6 edge-sharing octahedra along the *c*-axis that form parallel slabs but with different stacking arrangement. Delmas et al. proposed the structural classification for layered A_xTMO_2 (A = alkaline metal, TM = transition metal) materials using O2, O3 and P2, etc., where the letter indicates the form of coordination for A site (O: octahedral, P: prismatic) and the number (2 or 3) indicates the number of different $(TMO_2)_n$-layers per cell unit.[7]

Among these layered oxides, the P2 and O3-type Na_xMnO_2 compounds have garnered greater interest due to their superior electrochemical behavior and the low-cost of Mn. Compared with the O3 structure, the P2-type Na_xMnO_2 materials generally exhibit better electrochemical performance because of its low diffusion barrier for Na ions (**Scheme S1**) and applicable phase stability.[4,8] However, when P2-type Na_xMnO_2 is employed as a cathode material, the extraction of Na^+ at high voltage usually causes drastic structural changes, and the insertion of Na^+ at low voltage results in large Jahn-Teller distortions induced by Mn^{3+} ions, thus preventing reversible desodiation and sodiation upon long cycles.[9-11] For the O3-type Na_xMnO_2, the sufficient Na ions reserved in alkaline layer guarantees the Na supply upon long cycles, which is an advantage for commercial applications.[12] However, the structural stability of the O3

phase is worse than that of P2 phase, which arises from the inevitable complex phase transition under ambient condition.[13]

To overcome the above bottlenecks of pure P2- or O3-type Na_xMnO_2 cathodes, multiple-phase composites were proposed to enhance the physical and electrochemical properties .[14,15] Nonetheless, the combination of P2- and O3-type materials still suffer from irreversible structural transition that results in large capacity loss during long cycles.[14] In recent works, chemical substitution by inactive elements has been introduced as a modification method to improve structural stability and promote the cycling performance of Na_xMnO_2 materials[16,17]. For instance, Bruce et al. have used Mg substitution in P2-$Na_{0.67}Ni_{0.3-x}Mg_xMn_{0.7}O_2$ to inhibit the irreversible P2-O2 phase transition and optimize the reversible P2-OP4 transition.[18] Therefore, chemical doping is perhaps a rational route to achieve better electrochemical performance for the multiple-phase composite cathodes.

In this work, we develop a novel Ti-substituted Li-containing P2/O3-intergrown $Na_{0.8}Li_{0.27}Mn_{0.68}Ti_{0.05}O_2$ (P2/O3-NLMTO) cathode material for SIBs, which demonstrates highly reversible structural evolution upon Na^+ intercalation and de-intercalation. The oxygen redox capacity in P2/O3-NLMTO, compared with that of Ti-free $Na_{0.8}Li_{0.27}Mn_{0.73}O_2$ (P2/O3-NLMO), has been effectively promoted by increasing the electron density around oxygen ions, yet without sacrificing oxygen redox reversibility. Furthermore, the notorious Mn^{3+}/Mn^{4+} redox at low-voltage region has been greatly suppressed after Ti substitution. Ex-situ HRTEM and ^7Li solid-state NMR studies were employed to probe the crystal structure and the fate of lithium atoms,

revealing retarded surface crack and lithium loss during cycling. These findings could offer practical guidelines for formulating rational strategies to improve structure rigidity and electrochemical performance of Mn-based cathode materials in SIBs.

2. EXPERIMENTAL SECTION

2.1. Materials synthesis. The $Na_{0.8}Li_{0.27}Mn_{0.73}O_2$ (P2/O3-NLMO) and $Na_{0.8}Li_{0.27}Mn_{0.68}Ti_{0.05}O_2$ (P2/O3-NLMTO) samples were synthesized by using a facile solid-state reaction. $Na_2CO_3 \cdot H_2O$ (Aladdin, 99.999%), Li_2CO_3 (Aladdin, 99.99%), MnO_2 (Aladdin, 99.95%), and TiO_2 (Aladdin, 99.99%) powders were used with stoichiometric amounts. Excess of Na and Li sources (3%) were used to compensate for their loss at high temperature. The starting materials were thoroughly mixed by wet ball milling in ethanol at 250 rpm for 2 h and then dried at 70 ℃ for 30 min in air. After pressing into pellets, the precursor mixture was calcined in air at 700 ℃ for 12 h with a heating rate of 2 ℃/min and then naturally cooled down to room temperature. The final product was ground in an agate mortar and stored in an Ar-filled glovebox before use.

2.2. Electrochemical testing. Both P2/O3-NLMO and P2/O3-NLMTO laminated electrodes consisted of 80 wt% active material, 10 wt% Super P (conductive additives), and 10 wt% PVDF (polyvinylidene fluoride) binder. Note that carbon nanotube conductive additives were used in all electrodes subjected to EPR experiments in order to avoid the interference of strong signal arising from Super P. The mass loading of cathode materials on the electrode was 3.0-4.0 mg cm^{-2}. Metallic sodium and glass fibers were used as the negative electrode and separator, respectively. The electrolyte

was 1.0 M $NaPF_6$ in ethylene carbonate (EC) and propylene carbonate (PC) [1:1 in volume] with 5% fluorinated ethylene carbonate (FEC) as an electrolyte additive. CR2032-type coin cells were then assembled in an Ar-filled glovebox (O_2, H_2O < 0.1 ppm). The assembled electrodes were dried overnight at 110 ℃ in a vacuum oven before electrochemical measurements. Galvanostatic charge-discharge measurements at room temperature were conducted using a Land 2001A battery test system. The cyclic voltammetry (CV) with 0.05 mV s^{-1} and electrochemical impedance spectra (EIS) with frequency range from 0.01 Hz to 100 kHz were tested by a CHI660e electrochemical workstation. For all ex-situ characterizations, the cells were held for at least 6 h after reaching the given states-of-charge (SoC) and then disassembled inside an Ar-filled glovebox. The electrodes were then washed with dimethyl methyl carbonate (DMC) for three times and dried for at least 12 h in Ar-filled glovebox.

2.3. Materials Characterization. The crystal structures of the pristine cathode powder were characterized by X-ray diffraction (XRD) in the synchrotron beam line BL14B at Shanghai Synchrotron Radiation Facility (λ = 0.68889Å). The synchrotron XRD patterns were refined using FullProf Suite software. The ex-situ laboratory XRD patterns were conducted on instrument (Smartla SE, Rigaku) with Cu-Kα radiation (V = 40 kV, I = 40 mA, λ = 1.5406 Å). The chemical composition of samples was determined via inductively coupled plasma-atomic emission spectrometry (ICP-AES, Agilent ICP-OES 730). The scanning transmission electron microscopy (STEM) and high-resolution TEM (HRTEM) analyses were performed on EI Tecnai G2 F200 and FEI TECNAI G2 F20 microscopes. The HRTEM patterns were analyzed with the Gatan

DigitalMicrograph program. The X-ray photoelectron spectroscopy (XPS) measurements of the as-synthesized samples were conducted using an AXIS Ultra DLD spectrometer (SHIMADZU Ltd., Japan).

The soft X-ray adsorption spectroscopy (sXAS) experiments were carried out at Shanghai Synchrotron Radiation Facility (BL08U). Total-electron-yield (TEY) mode (the probe depth is about 10 nm) was used to obtain the O *K*-edge and Mn *L*-edge sXAS spectra. All sXAS experiments were performed under ultrahigh vacuum (10^{-7} Torr) condition at room temperature. Hard X-ray absorption spectroscopy (hXAS) experiments at Mn *K*-edge (E_0 = 6539 eV) were monitored at Shanghai Synchrotron Radiation Facility (BL14W1), operating at 3.5 GeV under "top-up" mode with a constant current of 220 mA. The hXAS data was collected under transmission mode and the energy was calibrated according to the absorption edge of pure Mn foil. All the data processing performed prior to analysis, including background subtraction, energy calibration, normalization and Fourier transformation was performed using the Athena program. To get the X-ray absorption near edge structure (XANES) spectra, the hXAS data were processed by background subtraction and normalization procedures. In order to present effective radial distribution function, the *k* space has been selected to between 2 and 12 $Å^{-1}$, and the Rbkg value has been set to 1.0 in the Fourier transformed extended X-ray absorption fine structure (EXAFS) spectra. Note that the phase correction was not applied in these FT spectra, thus the distance value are not the accurate bond lengths.

^{7}Li magic-angle spinning (MAS) solid-state NMR experiments were performed on a 2.35 T Bruker AVANCE II spectrometer operating at a ^{7}Li Larmor frequency of 38.78

MHz and equipped with a 2.5 mm triple resonance HXY MAS probe used in double-resonance mode. Temperature was calibrated by measuring the ^{1}H paramagnetic shift difference of a mixture of ferrocene and nickelocene solids. The temperature of tested samples was maintained at 309 K using temperature regulation system (BVT and BCU unit). The mass loading of cathode materials on the electrode was 6.0-7.0 mg cm^{-2} for NMR experiments. The cycled electrode materials were scraped from Al foil in Ar-filled glovebox and packed into 2.5 mm zirconia rotors and spun at the frequency of 25 kHz. The ^{7}Li pj-MATPASS (pj = projection, MAT: magic-angle turning, PASS: phase-adjusted sideband separation)[19] spectra were acquired using $\pi/2$ pluse of 1.8 μs and result from averaging of 5k-55k transients with a recycle delay of 40 ms. Chemical shifts were referenced to 1 M LiCl solution at 0 ppm.

Continuous-wave electron paramagnetic resonance (CW-EPR) spectra were acquired on a Bruker EMX plus 10/12 spectrometer in X-band (9.4 GHz), using a perpendicular-mode microwave cavity and an Oxford ESR910 liquid helium cryostat. The microwave power and modulation amplitude were respectively set to 0.1 mW and 2 G; microwave frequency and modulation frequency were respectively set to 9.647 G and 100 kHz; and temperature was set to 90 K.

3. RESULTS AND DISCUSSION

3.1. Structure Characterizations. Synchrotron XRD (SXRD) was utilized to identify the crystal structures of the obtained P2/O3-NLMO and P2/O3-NLMTO, as shown in **Figures 1**a and b. As expected, the diffraction peaks of the two samples can both be well indexed to a mixture of hexagonal lattices with space groups of $P6_3/mmc$ (P2) and

$R\bar{3}m$ (O3). According to the refined results of **Table S1, Table S2** and previous studies, [20,21] we believe that most of the Li ions enter the transition-metal sites to generate the major P2 phase, and residual Li ions occupy the Na sites to produce a small amount of O3 phase. It is noted that a low-intensity peak at 9.84° (marked with star) is observed for P2/O3-NLMO and P2/O3-NLMTO, which can be assigned to the long range in-plane ordering between Li^+ and Mn^{4+} ($\sqrt{3}a\times\sqrt{3}a$-type supercell).[22] The calculated crystallographic data of samples are presented in **Tables S3**. The results demonstrate that the relative ratio between P- and O-type phases is 98.08% (P2): 1.92% (O3) for P2/O3-NLMO and 97.84% (P2): 4.44% (O3) for P2/O3-NLMTO, respectively. According to previous work, an intergrowth structure can ameliorate complicated phase transitions and accompanied large volume variation upon cycling,[23-25] therefore the slightly higher proportion of O3 phase in P2/O3-NLMTO than in P2/O3-NLMO may indicates alleviated structure distortion and volume change in NLMTO during cycling. In addition, the chemical components of the as-prepared P2/O3-NLMO and P2/O3-NLMTO were evaluated via ICP by fixing the Mn content as a reference due to its non-volatility. The results (**Table S4**) suggest that the atomic ratios of the obtained-samples are consistent with the expected theoretical values.

To investigate the morphology and microstructure, detailed TEM and HRTEM analyses on the obtained P2/O3-NLMO and P2/O3-NLMTO were performed. The TEM images in **Figure 1**c and **Figure S1**a all illustrate hexagonal-shape particles with an average size of 0.5-1.5 μm, which is consistent with the hexagonal symmetry of the lattice. The HRTEM image in **Figure 1**d manifests two sets of clear lattice fringes,

directly showing the intergrowth of P2 and O3 structure at atomic scale.[14] The coexistence of P2 and O3 phases in P2/O3-NLMO is also observed in **Figure S1**b. Due to the low content of O3 phase, the major atomic structure of P2/O3-NLMTO shown in

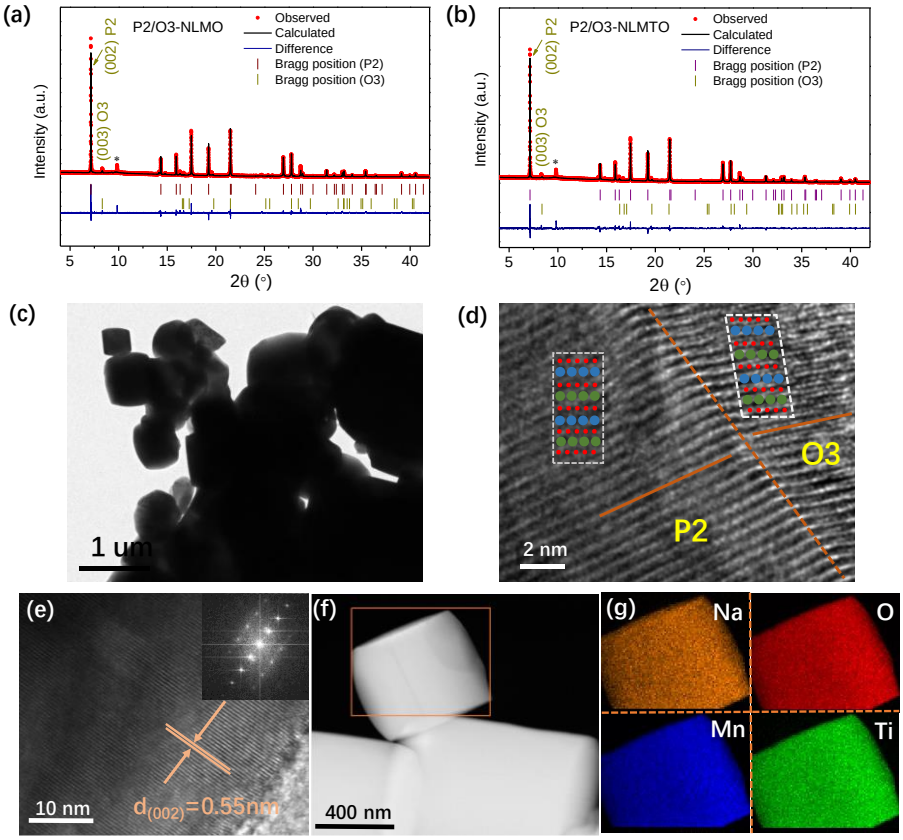

Figure 1. Synchrotron XRD patterns and the corresponding Rietveld refinement of (a) P2/O3-NLMO and (b) P2/O3-NLMTO with P2+O3 mixed phase. (c) TEM and (d) HRTEM image of P2/O3-NLMTO with intergrown P2+O3 phase, (e) HRTEM image of P2/O3-NLMTO presenting the major P2 phase, (f) TEM image and (g) the corresponding EDS mapping of a well ground NLMTO sample.

Figure 1e is still P2-type with a large interplanar distance of 0.55 nm corresponding to the *d*-spacing of (002) plane. Moreover, the energy dispersive spectroscopy (EDS)

mappings of P2/O3-NLMTO in **Figures 1**f and g display the homogeneous distribution of Ti, Na, Mn, and O elements on the sample surface. Furthermore, to confirm that Ti-doping uniformly occurs in the bulk material, XPS depth profiles were also collected (**Figure S2**). With increasing detection depth, the intensity of Ti 2p XPS peaks remain the same, thus suggesting the uniform Ti^{4+} distribution from the material surface to the bulk.

3.2. Electrochemical Properties. The electrochemical properties of the designed P2/O3-NLMTO and P2/O3-NLMO were gauged in Na half cells between 2.0 and 4.3 V *vs.* Na^+/Na. **Figure 2** shows the initial galvanostatic charge profiles and cycling performance of the P2/O3-NLMO and P2/O3-NLMTO electrodes at a current density of 20 mA g^{-1} between 2.0 and 4.3 V (*vs.* Na^+/Na). Similar to other reported layered Na_xMnO_2 cathodes containing pure Mn^{4+},[26,27] the initial charging curves of P2/O3-NLMO and P2/O3-NLMTO show a long plateau, which is likely due to the evolution of oxygen. Considering that the Mn^{4+} is unlikely to be oxidized to Mn^{5+} below 4.3 V, the initial extraction process of Na^+ results from pure oxygen oxidation. Interestingly, the initial charging capacity of the P2/O3-NLMTO electrode (127.9 mAh g^{-1}) is higher than that of P2/O3-NLMO (111.9 mAh g^{-1}), implying an increased anionic activation process. The CV curves in initial cycle are shown in **Figure S3**. Apparently, compared to P2/O3-NLMO, P2/O3-NLMTO exhibits enhanced oxidation peak above 3.3 V, furtherly suggesting that Ti substitution activates the reactivity of oxygen. After the activation process, the P2/O3-NLMTO electrode exhibits an outstanding performance in the following cycling, as shown in **Figure 2**. The initial discharge capacity of P2/O3-

NLMTO is 143.2 mAh g^{-1} and the remained capacity after 50 cycles is 112.6 mAh g^{-1} (90.7% capacity retention as compared to the second cycle). By contrast, the discharge capacity drops from 120.2 mAh g^{-1} to 95.3 mAh g^{-1} for the Ti-free P2/O3-NLMO sample. The electrochemical impedance spectra (EIS) of pristine electrodes displaying in **Figure S4** demonstrate lower charge-transfer impedance (R_{ct}) in P2/O3-NLMTO, thereby exhibiting better Na^+ diffusion rate.

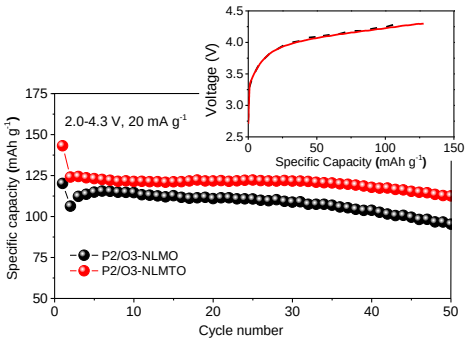

Figure 2. Electrochemical performance and initial charge profiles (insert) of P2/O3-NLMO and P2/O3-NLMTO between 2.0 and 4.3 V, measured at 20 mA g^{-1}.

The voltage profiles of the materials in different cycles at 20 mA g^{-1} are depicted in **Figure 3**. In contrast to the initial charge profile, the second charge curve exhibits two stages with a slope at low voltage and a plateau region above 3.3 V, which is related with the oxidation of Mn^{3+} and O-related anionic process, respectively.[28,29] Intriguingly, the high-potential oxygen oxidative profiles of P2/O3-NLMTO are stable in the following cycles, while the oxygen redox process changes greatly in P2/O3-NLMO, demonstrating a favorable reversibility of the cycling process after Ti substitution.

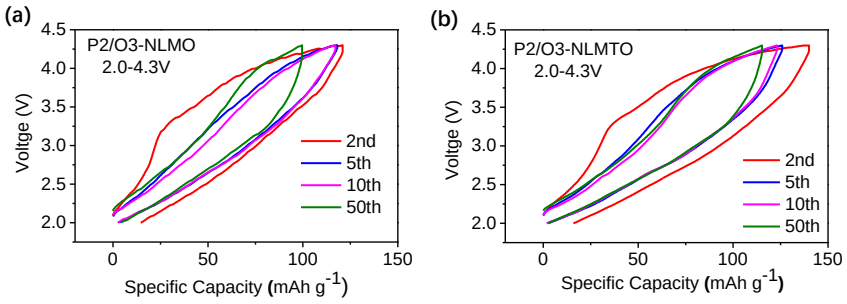

Figure 3. Representative charge/discharge profiles of (a) P2/O3-NLMO and (b) P2/O3-NLMTO electrodes under different numbers of cycle at a current density of 20 mA g^{-1} between 2.0 and 4.3 V.

3.3. Charge Compensation Mechanism Studies. To study the oxygen–related charge compensation process of P2/O3-NLMO and P2/O3-NLMTO, spectroscopic studies were conducted via O and Mn soft X-ray absorption spectroscopy (sXAS) (**Figure 4**a and c). A soft X-ray in energy range from 522 eV to 550 eV excites filled O 1*s* electrons to empty O 2*p* (*K*-edge), allowing direct probe of O unoccupied states.[30] The O *K*-edge sXAS is dominated by a broad feature peak above 535 eV, which is attributed to the excitation from the O 1*s* orbital to the hybridized orbital of transition metal (TM) 4*sp* and O 2*p*. The pre-edge peaks at lower energy (529.0 and 531.4 eV) are associated to the transition from the O 1*s* orbital to the unoccupied hybridized orbital of TM 3*d* and O 2*p*.[31,32] In addition, the extra peak at 533.2 eV is assigned to carbonate (Na_2CO_3 or Li_2CO_3) in the surface. [33] The TEY mode sXAS spectra of Mn *L*-edge shown in **Figure 4**c allow one to assign the valence state of Mn ions. The peaks at 642.8 eV and 640.4 eV correspond to Mn^{4+}, whereas the peak at 641.0 eV corresponds to Mn^{3+} ions, and the peak at 639.4 eV is associated with Mn^{2+}.

As shown in **Figure 4**a, for both Ti-free and Ti-substituted samples, the changes in

the intensity of pre-edge peak at 531.4 eV show a similar trend, displaying an increase of hole state when charging to 4.3 V. Although the presence of electron holes on oxygen cannot be explained by O sXAS alone, the Mn *L*-edge spectra show no change beyond Mn^{4+} after charging to 4.3 V (**Figure 4**c), thus we conclude that the increased hole states must be located on the O anions.[34] In particular, compared with the spectra of P2/O3-NLMO, the pre-edge peak of P2/O3-NLMTO increases more obviously upon charging, suggesting the greater oxygen electron contribution at highly desodiated state. Considering that there is no valence electron in the $3d^0$ configuration of Ti^{4+}, we perceive that Ti^{4+} is inactive during charging process. Compared with Mn-O bond, the electrons in Ti-O bond are closer to oxygen atoms, which increases the electron density around oxygen (as illustrated in **Figure 4**b) and thus promote the oxidation of oxygen ion.[35-37] This result is consistent with the much higher capacity at high-voltage plateau region in P2/O3-NLMTO compared with P2/O3-NLMO.

Upon the reverse discharge process, the intensity of the pre-edge peak in the O K-edge spectra decrease greatly and the broad peak above 535 eV shifts to lower energy for both P2/O3-NLMO and P2/O3-NLMTO samples, which reveals the elongation of TM-O bond owing to the expansion of Mn ions by gaining electrons. The Mn *L*-edge spectra in **Figure 4**c also suggest the reduction of Mn^{4+} to Mn^{3+} and Mn^{2+} after discharging. Note that the O K-edge spectra display similar peak intensity for both samples. This is due to the fact that the extra oxidized O^{2-} in P2/O3-NLMTO is reversibly reduced during the discharge process. Such reversibility of oxygen redox ensures the overall capacity stability during cycle.

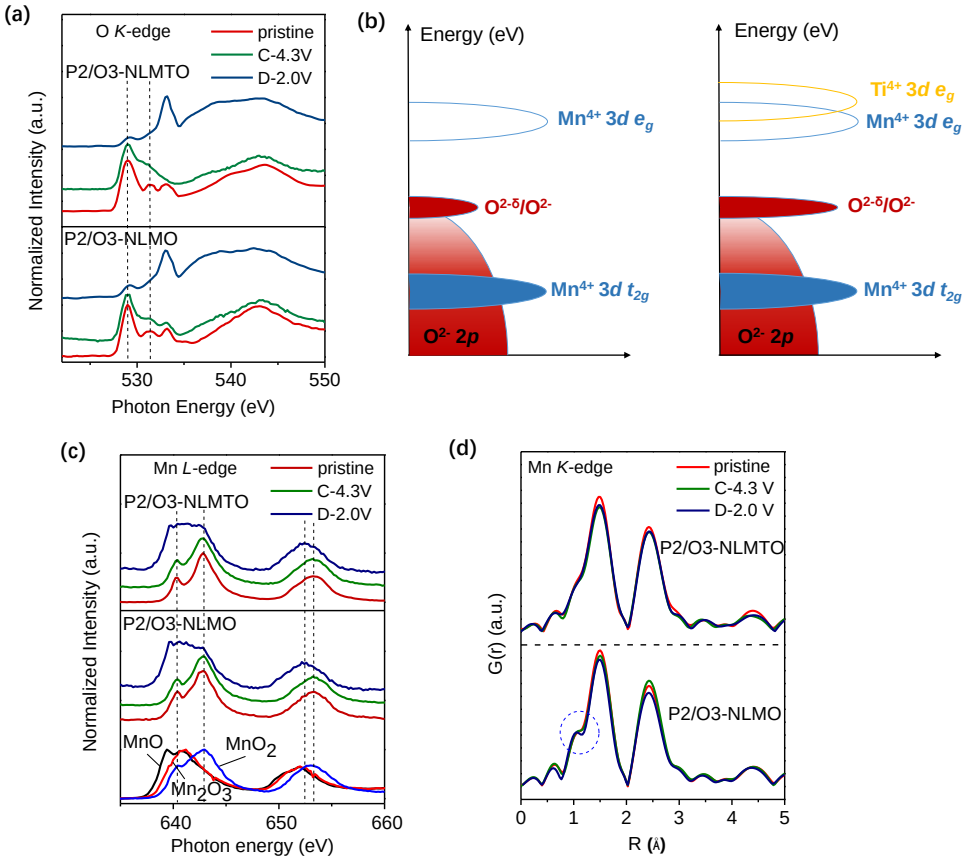

Figure 4. (a) O K-edge sXAS spectra under TEY mode and (b) Schematic electronic structures of P2/O3-NLMO and P2/O3-NLMTO. (c) Mn L-edge sXAS spectra under TEY mode and (d) Fourier-transformed Mn K-edge EXAFS spectra of P2/O3-NLMO and P2/O3-NLMTO; all spectra collected on pristine, fully charged (C-4.3V), and fully discharged (D-2.0V) states during the first cycle.

Considering the limited detective depth of sXAS, the normalized X-ray absorption near-edge structure (XANES) spectra and the extended X-ray absorption fine structure (EXAFS) analyses were conducted at Mn *K*-edge to explore the bulk oxide state of Mn upon first cycle for the two samples. The XANES spectra at Mn *K*-edge and the local magnified region are presented in **Figure S5**. The shape and peak position of Mn XANES shows no significant changes until charged to 4.3 V, implying that Mn ions are

electrochemically inactive as the tetravalent state for both samples. Upon discharge, the spectrum of P2/O3-NLMO shifts to a lower energy position, while the spectrum of P2/O3-NLMTO stays unchanged, which implies the lower Mn valence in non-substituted sample. From the Fourier-transformed Mn *K*-edge EXAFS spectra shown in **Figure 4**d, the two main peaks, respectively associated with Mn-O bonds and Mn-TM bonds,[38,39] are all observable in two cases. Notably, for the P2/O3-NLMO in the fully discharged state, an obvious peak at 1.07 Å (in dashed circle) originating from Jahn-Teller distortion is clearly witnessed.[40] However, this peak is hardly observed in discharged P2/O3-NLMTO, evidencing the suppressed reduction of Mn^{4+} to Mn^{3+} by Ti substitution. This phenomenon can be explained by the retarded lattice oxygen loss during the initial charge process based on the intuitive electroneutrality principle. In fact, the restrained Mn^{3+}-triggered Jahn-Teller distortions and lattice oxygen loss by utilizing Ti substitution have also been reported previously in Zhou's work despite the fact that only P2 phase was explored.[29]

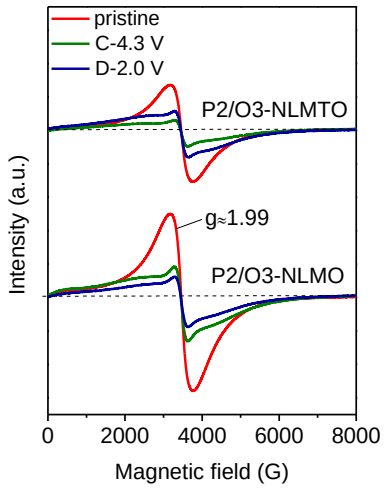

Figure 5. Perpendicular-mode EPR spectra of P2/O3-NLMO and P2/O3-NLMTO electrodes in

pristine (red), fully charged (C-4.3V, green), and fully discharged (D-2.0V, blue) state.

To further investigate the electronic state of Mn and O ions before and after Ti substitution, the EPR tests were performed under perpendicular mode to probe the electronic state of Mn and O ions (**Figure 5**). Both pristine P2/O3-NLMO and P2/O3-NLMTO display a signal with Lorentzian shape centered at g ≈ 1.99, which is ascribed to Mn^{4+} ions with antiferromagnetically coupled Mn^{4+}-O-Mn^{4+} cluster.[41,42] Intriguingly, the symmetrical EPR signal of P2/O3-NLMTO is weaker than that of P2/O3-NLMO. We note that there are pure MnO_6 structures in P2/O3-NLMO sample, while 30% Mn^{4+}-O bonding is influenced by 5% Ti substitution in Mn site in P2/O3-NLMTO, resulting in the subdued signal of the latter one. After charging to 4.3 V, the EPR signal representing Mn^{4+}-O coupling decays for the two materials, arising from the decreased coupling between Mn^{4+} and oxidized oxygen species $O^{2-\delta}$.[42] Meanwhile, a broad symmetrical line appears as a shoulder on the narrow Lorentzian line with g ≈ 1.99, which may be assigned to a new Mn^{4+}-O coupling environment with much different electron-electron dipolar interaction. The detailed structure investigation is still in progress to draw an explicit explanation. Importantly, at fully discharged state, although the $O^{2-\delta}$ ions were reversibly reduced, the narrow EPR signal keeps decreasing in P2/O3-NLMO electrode, which might be attributed to the high amount of EPR-silent Mn^{3+} ions produced during the Na^+ reinsertion process. In contrast, the corresponding signal increases appreciably in P2/O3-NLMTO at discharged state, indicating the alleviated charge compensation contribution from Mn^{3+}/Mn^{4+} couple. Such result is

also consistent with the result of XANES and EXAFS analysis.

3.4. Structure Evolution. To further monitor the structure rigidity of P2/O3-NLMO and P2/O3-NLMTO during cycling, ex-situ high-resolution transmission electron microscopy (HRTEM) analyses were performed at different states-of-charge (SoC). In **Figures 6**a and e, the two electrode materials both show smooth integrated structure in surface upon charging to 4.0 V. However, **Figures 6**b and c reveal that obvious cracks are formed in no-substituted P2/O3-NLMO compound when further charging to 4.3 V, whereas no apparent crack is observed for charged P2/O3-NLMTO (**Figures 6**f, g). This clear difference in the surface structure is indeed a result of the structure rigidity induced by Ti substitution. Previous reports have shown that at high desodiation level, layered sodium manganese oxides and lithium manganese oxides experience grain cracks, which is attributed to an increase of interfacial microstrain and unavoidable volume shrink owing to phase transition and distorted intrinsic oxygen framework.[11,43-46] We believe that the small amount of Ti^{4+} in the transition metal layer can greatly promote physical strength of the particles due to the "pillaring effect" of inactive Ti^{4+}.[47] Furthermore, Ti-substitution increases the proportion of interlocked O3 (**Table S3**), which could alleviate the volume change and phase instability of P2 domain during cycling, thus effectively suppressing the formation of crack. As shown in **Figure S6**, all the diffraction patterns almost have no changes expect for the peak position, indicating a solid-solution process upon cycling. In addition, a detailed comparison of the shifts of $P2_{(002)}$ peak demonstrates an extremely small change of *c* value of P2 domain after Ti substitution. After the subsequent discharge process, as shown in

Figures 6d and h, microcracks are still detected on the surface of P2/O3-NLMO, in sharp contrast to the smooth surface of Ti-substituted sample, which prove that Ti-substitution can efficiently suppress the irreversible structure collapse of P2/O3-NLMO samples.

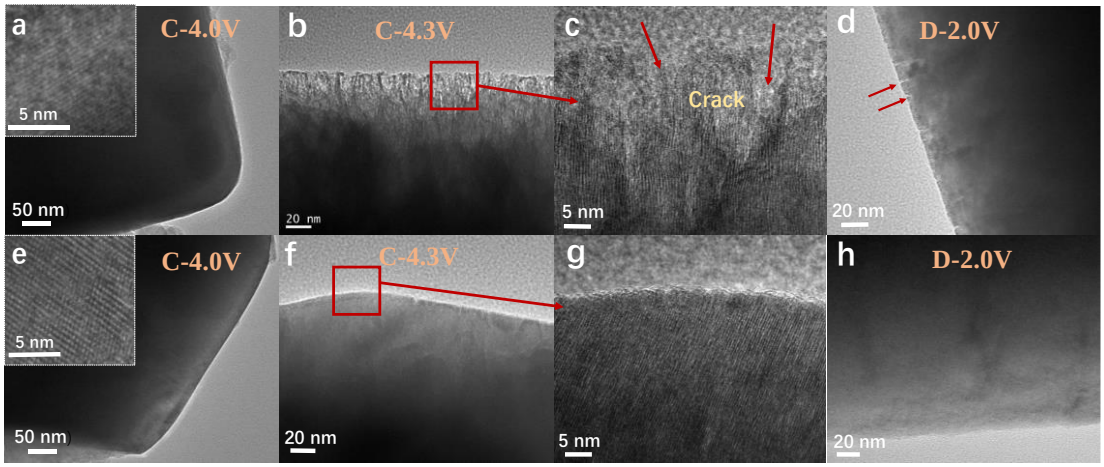

Figure 6. (a)-(d) Ex-situ HRTEM images of the P2/O3-NLMO electrodes after (a) charging to 4.0 V, (b) (c) charging to 4.3 V in different magnification, and (d) discharging to 2.0 V. (e)-(h) HRTEM images of P2/O3-NLMTO after (e) charging to 4.0 V, (f) (g) charging to 4.3 V in different magnification, and (h) discharging to 2.0 V.

In the past decade, experimental and theoretical studies have proved that the anionic redox in oxide cathode materials arises from the presence of oxygen lone-pair,[30,48-51] that is associated with the 'Na-O-Li' configuration in P2/O3-NLMO and P2/O3-NLMTO in our case. Moreover, the local ordering of Li^{+}/Mn^{4+} in TM layer may lock the surrounding O atoms and retard their gliding, which in turn delays the phase transition. Therefore, it is important to follow the fate of Li^{+} ions during cycling as they play a critical role in the O-redox reaction. ^{7}Li NMR is a sensitive probe of the local

atomic environment of Li^+ ions and thus is a vital method to quantitatively monitor changes of Li species during cycling. To this end, 2D pj-MATPASS experiments were performed to disentangle the multiple resonances of ^{7}Li sites. The 2D pj-MATPASS spectra of P2/O3-NLMTO electrode in pristine state are plotted in **Figure S7** to explain the process of tilt transformation and sum projection. The isotropic slices of ^{7}Li 2D pj-MATPASS NMR spectra obtained after spectral shearing along the F2 dimension for P2/O3-NLMO and P2/O3-NLMTO under various electrochemical states are displayed in **Figure 7**. Generally, the signals resonating at ~1900 ppm and ~1500 ppm are tentatively assigned to Li ions within the TM layer, while the signal at ~750 ppm is attributed to Li ions in the Na layer.[20,28,42] In addition, the signal observed at 0 ppm can be assigned to diamagnetic Li-containing species (such as Li_2CO_3 and LiF) residing on the surface of particles. The resulting spectra are normalized according to the number of scans and the mass, permitting semi-quantified comparison. As shown in **Figure 7**, the relative content of Li atoms in TM layer of the pristine electrodes increases from 65.8% to 77.9% after Ti substitution. It is also noteworthy that cycling the electrodes greatly reduced the total signal of Li^+ ions and also altered the distribution of Li^+ ions among TM layers and Na layers. Although we cannot rule out the effect of faster T_2 relaxation upon cycling, these results still give useful insights when considering the difference in between the two series of samples. In particular, for the samples that went through 25 cycles, the relative amount of Li in TM layers and the total amount of Li atoms in P2/O3-NLMTO were almost twice that of the Ti-free P2/O3-NLMO, which may be attributed to the stronger Na-O-Li bonding after Ti substitution. Because Li^+

ions in the TM layers are key stabilizers of materials and their loss upon long-term cycling is one of the most important reasons of capacity degradation, our results of ^{7}Li pj-MATPASS NMR further confirm the positive effect of Ti substitution into Mn on the structural stability of P2/O3 biphasic NLMO.

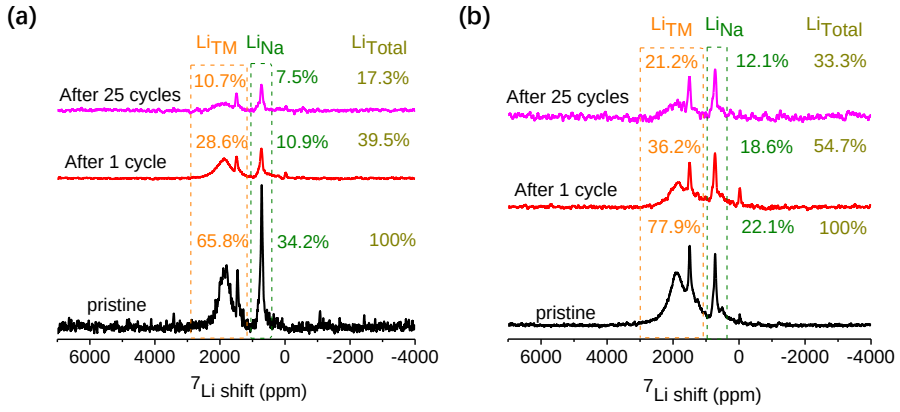

Figure 7. Isotropic ^{7}Li pj-MATPASS NMR spectra of (a) P2/O3-NLMO and (b) P2/O3-NLMTO electrodes under various electrochemical states: pristine (black), after first cycle (red), and after 25 cycles (pink). All spectra have been normalized according to the number of scans and the mass. Spectra were obtained by tilt transformation and sum projection of the 2D pj-MATPASS raw spectra. An example of such processing is shown in **Figure S7**.

4. CONCLUSIONS

In this work, we successfully ameliorate the cyclic performance of P2/O3-$Na_{0.8}Li_{0.27}Mn_{0.73}O_2$ cathode material by a facile partial Ti-substitution strategy. The comparison of electrochemical performance between Ti-substituted P2/O3-$Na_{0.8}Li_{0.27}Mn_{0.68}Ti_{0.05}O_2$ and non-substituted counterpart clearly proves that the incorporation of Ti-substitution improves the initial discharge specific capacity and also the capacity retention after long cycles. By increasing the electron density around O

ions in Ti-O bonding upon charge, as well as inhibiting the problematic Jahn-Teller effect of Mn^{3+} during discharge, Ti-incorporation effectively promotes the oxygen electron contribution to the redox reaction without sacrificing O-redox reversibility. Especially, analyses based on ex-situ HRTEM and ^{7}Li solid-state NMR characterizations reveal that multiple factors are important to achieve the structure stability for Ti-substituted materials: (1) the irreversible surface crack is eliminated within a voltage range of 2.0-4.3 V; (2) lithium loss in the lattice is effectively alleviated and lithium ions in TM layer is well maintained. Altogether, Ti-substitution is an efficient and broadly applicable strategy for improving the practical performance of Mn-based P2/O3 biphasic cathodes for sodium-ion battery.

ASSOCIATED CONTENT

The Supporting Information is available free of charge at **Supporting Information**.

Schemes, TEM, XPS, CV, XANES and NMR curves (PDF)

AUTHOR INFORMATION

Corresponding Authors

Chao Li − *East China Normal University, Shanghai, P. R. China;* orcid.org/0000-0002-0153-7825; Email: lchao@phy.ecnu.edu.cn

Ming Shen − *East China Normal University, Shanghai, P. R. China;* orcid.org/0000-0003-1343-2761；Email: mshen@phy.ecnu.edu.cn.

Author Contributions

Bei Hu - *East China Normal University, Shanghai, P. R. China;* orcid.org/0000-0002-8506-0007

Fushan Geng - *East China Normal University, Shanghai, P. R. China*

Chong Zhao - *East China Normal University, Shanghai, P. R. China*

Bertrand Doumert - *Univ. Lille, CNRS, Centrale Lille, Univ. Artois, UMR 8181, UCCS – Unité de Catalyse et de Chimie du Solide, F-59000 Lille, France; Univ. Lille, CNRS-2638, Fédération Chevreul, F-59000 Lille, France.*

Julien Trébosc - *Univ. Lille, CNRS, Centrale Lille, Univ. Artois, UMR 8181, UCCS – Unité de Catalyse et de Chimie du Solide, F-59000 Lille, France; Univ. Lille, CNRS-2638, Fédération Chevreul, F-59000 Lille, France.*

Olivier Lafon - *Univ. Lille, CNRS, Centrale Lille, Univ. Artois, UMR 8181, UCCS – Unité de Catalyse et de Chimie du Solide, F-59000 Lille, France; Institut Universitaire de France*

Bingwen Hu - *East China Normal University, Shanghai, P. R. China;* orcid.org/0000-0003-0694-0178.

The manuscript was written through contributions of all authors. All authors have given approval to the final version of the manuscript. ‡These authors contributed equally.

Notes

The authors declare no competing financial interest.

ACKNOWLEDGEMENTS

This work was supported by National Natural Science Foundation of China (Nos.

21902049, 21703068, 21872055, and 21874045), Shanghai Sailing Program (19YF1413000) and the Fundamental Research Funds for the Central Universities. We also acknowledge the support from the Steady High Magnetic Field Facilities of High Magnetic Field Laboratory (CAS) for the EPR experiments, and the support from Shanghai Synchrotron Radiation Facility for the SXRD (BL14B), sXAS (BL08UA) and XANES (BL14W1) experiments. B. Hu, F. Geng, and C. Zhao are thankful for the financial support from the graduate students overseas visiting project of East China Normal University. Chevreul Institute (FR 2638), Ministère de l'Enseignement Supérieur, de la Recherche et de l'Innovation, Hauts-de-France Region and FEDER are acknowledged for supporting and funding partially this work. O. Lafon acknowledges the financial support from contract ANR-18-CE08-0015-01 (ThinGlass) and Institut Universitaire de France (IUF).

REFERENCES

(1) Dunn, B.; Kamath, H.; Tarascon, J. M. Electrical Energy Storage for the Grid: A Battery of Choices. *Science* **2011**, *334*, 928-935.

(2) Kundu, D.; Talaie, E.; Duffort, V.; Nazar, L. F. The Emerging Chemistry of Sodium Ion Batteries for Electrochemical Energy Storage. *Angew. Chem. Int. Ed.* **2015**, *54*, 3431-3448.

(3) Li, Z.; Young, D.; Xiang, K.; Carter, W. C.; Chiang, Y. Towards High Power High Energy Aqueous Sodium-Ion Batteries: The $NaTi_2(PO_4)_3/Na_{0.44}MnO_2$ System. *Adv. Energy Mater.* **2013**, *3*, 290-294.

(4) Han, M. H.; Gonzalo, E.; Singh, G.; Rojo, T. A Comprehensive Review of Sodium

Layered Oxides: Powerful Cathodes for Na-ion Batteries. *Energy Environ. Sci.* **2015**, *8*, 81-102.

(5) Clément, R. J.; Bruce, P. G.; Grey, C. P. Review—Manganese-Based P2-Type Transition Metal Oxides as Sodium-Ion Battery Cathode Materials. *J. Electrochem. Soc.* **2015**, *162*, A2589-A2604.

(6) Li, C.; Shen, M.; Hu, B.; Lou, X.; Zhang, X.; Tong, W.; Hu, B. High-Energy Nanostructured $Na_3V_2(PO_4)_2O_{1.6}F_{1.4}$ Cathodes for Sodium-Ion Batteries and a New Insight Into their Redox Chemistry. *J. Mater. Chem. A* **2018**, *6*, 8340-8348.

(7) Delmas, C.; Fouassier, C.; Hagenmuller, P. Structural Classification and Properties of the Layered Oxides. *Physica B+C* **1980**, *99*, 81-85.

(8) Guo, S.; Liu, P.; Yu, H.; Zhu, Y.; Chen, M.; Ishida, M.; Zhou, H. A Layered P2- and O3-Type Composite as a High-Energy Cathode for Rechargeable Sodium-Ion Batteries. *Angew. Chem. Int. Ed.* **2015**, *54*, 5894-5899.

(9) Yabuuchi, N.; Kajiyama, M.; Iwatate, J.; Nishikawa, H.; Hitomi, S.; Okuyama, R.; Usui, R.; Yamada, Y.; Komaba, S. P2-Type $Na_x[Fe_{1/2}Mn_{1/2}]O_2$ Made From Earth-Abundant Elements for Rechargeable Na Batteries. *Nat. Mater.* **2012**, *11*, 512-517.

(10) Hasa, I.; Buchholz, D.; Passerini, S.; Scrosati, B.; Hassoun, J. High Performance $Na_{0.5}[Ni_{0.23}Fe_{0.13}Mn_{0.63}]O_2$ Cathode for Sodium-Ion Batteries. *Adv. Energy Mater.* **2014**, *4*, 1400083.

(11) Pang, W. K.; Kalluri, S.; Peterson, V. K.; Sharma, N.; Kimpton, J.; Johannessen, B.; Liu, H. K.; Dou, S. X.; Guo, Z. Interplay between Electrochemistry and Phase Evolution of the P2-Type $Na_x(Fe_{1/2}Mn_{1/2})O_2$ Cathode for Use in Sodium-Ion Batteries.

Chem. Mater. **2015**, *27*, 3150-3158.

(12) Fouassier, C.; Delmas, C.; Hagenmuller, P. Evolution Structurale Et Proprietes Physiques Des Phases $AXMO_2$ (A = Na, K; M = Cr, Mn, Co) ($X \leqslant 1$). *Mater. Res. Bull.* **1975**, *10*, 443-449.

(13) Li, X.; Wu, D.; Zhou, Y.; Liu, L.; Yang, X.; Ceder, G. O3-Type $Na(Mn_{0.25}Fe_{0.25}Co_{0.25}Ni_{0.25})O_2$: A Quaternary Layered Cathode Compound for Rechargeable Na Ion Batteries. *Electrochem. Commun.* **2014**, *49*, 51-54.

(14) Lee, E.; Lu, J.; Ren, Y.; Luo, X.; Zhang, X.; Wen, J.; Miller, D.; DeWahl, A.; Hackney, S.; Key, B.; Kim, D.; Slater, M. D.; Johnson, C. S. Layered P2/O3 Intergrowth Cathode: Toward High Power Na-Ion Batteries. *Adv. Energy Mater.* **2014**, *4*, 1400458.

(15) Chen, X.; Zhou, X.; Hu, M.; Liang, J.; Wu, D.; Wei, J.; Zhou, Z. Stable Layered P3/P2 $Na_{0.66}Co_{0.5}Mn_{0.5}O_2$ Cathode Materials for Sodium-Ion Batteries. *J. Mater. Chem. A* **2015**, *3*, 20708-20714.

(16) Yoshida, H.; Yabuuchi, N.; Kubota, K.; Ikeuchi, I.; Garsuch, A.; Schulz-Dobrick, M.; Komaba, S. P2-Type $Na_{2/3}Ni_{1/3}Mn_{2/3-x}Ti_xO_2$ as a New Positive Electrode for Higher Energy Na-ion Batteries. *Chem. Commun.* **2014**, *50*, 3677-3680.

(17) Wang, P.; You, Y.; Yin, Y.; Wang, Y.; Wan, L.; Gu, L.; Guo, Y. Suppressing the P2-O2 Phase Transition of $Na_{0.67}Mn_{0.67}Ni_{0.33}O_2$ by Magnesium Substitution for Improved Sodium-Ion Batteries. *Angew. Chem. Int. Ed.* **2016**, *55*, 7445-7449.

(18) Singh, G.; Tapia-Ruiz, N.; Lopez Del Amo, J. M.; Maitra, U.; Somerville, J. W.; Armstrong, A. R.; Martinez De Ilarduya, J.; Rojo, T.; Bruce, P. G. High Voltage Mg-

Doped $Na_{0.67}Ni_{0.3-x}Mg_xMn_{0.7}O_2$ (X = 0.05, 0.1) Na-Ion Cathodes with Enhanced Stability and Rate Capability. *Chem. Mater.* **2016**, *28*, 5087-5094.

(19) Hung, I.; Zhou, L.; Pourpoint, F.; Grey, C. P.; Gan, Z. Isotropic High Field NMR Spectra of Li-Ion Battery Materials with Anisotropy >1 MHz. *J. Am. Chem. Soc.* **2012**, *134*, 1898-1901.

(20) Yang, L.; Li, X.; Ma, X.; Xiong, S.; Liu, P.; Tang, Y.; Cheng, S.; Hu, Y.; Liu, M.; Chen, H. Design of High-Performance Cathode Materials with Single-Phase Pathway for Sodium Ion Batteries: A Study On P2-$Na_x(Li_yMn_{1-y})O_2$ Compounds. *J. Power Sources* **2018**, *381*, 171-180.

(21) Li, Z.; Zhang, J.; Gao, R.; Zhang, H.; Zheng, L.; Hu, Z.; Liu, X. Li-Substituted Co-Free Layered P2/O3 Biphasic $Na_{0.67}Mn_{0.55}Ni_{0.25}Ti_{0.2-x}Li_xO_2$ as High-Rate-Capability Cathode Materials for Sodium Ion Batteries. *J. Phys. Chem. C* **2016**, *120*, 9007-9016.

(22) Yabuuchi, N.; Hara, R.; Kajiyama, M.; Kubota, K.; Ishigaki, T.; Hoshikawa, A.; Komaba, S. New O2/P2-type Li-Excess Layered Manganese Oxides as Promising Multi-Functional Electrode Materials for Rechargeable Li/Na Batteries. *Adv. Energy Mater.* **2014**, *4*, 1301453.

(23) Huang, Q.; Liu, J.; Zhang, L.; Xu, S.; Chen, L.; Wang, P.; Ivey, D. G.; Wei, W. Tailoring Alternating Heteroepitaxial Nanostructures in Na-ion Layered Oxide Cathodes Via an In-Situ Composition Modulation Route. *Nano Energy* **2018**, *44*, 336-344.

(24) Yabuuchi, N.; Hara, R.; Kajiyama, M.; Kubota, K.; Ishigaki, T.; Hoshikawa, A.;

Komaba, S. New O2/P2-type Li-Excess Layered Manganese Oxides as Promising Multi-Functional Electrode Materials for Rechargeable Li/Na Batteries. *Adv. Energy Mater.* **2014**, *4*, 1301453.

(25) de la Llave, E.; Talaie, E.; Levi, E.; Nayak, P. K.; Dixit, M.; Rao, P. T.; Hartmann, P.; Chesneau, F.; Major, D. T.; Greenstein, M.; Aurbach, D.; Nazar, L. F. Improving Energy Density and Structural Stability of Manganese Oxide Cathodes for Na-Ion Batteries by Structural Lithium Substitution. *Chem. Mater.* **2016**, *28*, 9064-9076.

(26) Rong, X.; Liu, J.; Hu, E.; Liu, Y.; Wang, Y.; Wu, J.; Yu, X.; Page, K.; Hu, Y.; Yang, W.; Li, H.; Yang, X.; Chen, L.; Huang, X. Structure-Induced Reversible Anionic Redox Activity in Na Layered Oxide Cathode. *Joule* **2018**, *2*, 125-140.

(27) Rong, X.; Hu, E.; Lu, Y.; Meng, F.; Zhao, C.; Wang, X.; Zhang, Q.; Yu, X.; Gu, L.; Hu, Y.; Li, H.; Huang, X.; Yang, X.; Delmas, C.; Chen, L. Anionic Redox Reaction-Induced High-Capacity and Low-Strain Cathode with Suppressed Phase Transition. *Joule* **2019**, *3*, 503-517.

(28) Yang, L.; Li, X.; Liu, J.; Xiong, S.; Ma, X.; Liu, P.; Bai, J.; Xu, W.; Tang, Y.; Hu, Y.; Liu, M.; Chen, H. Lithium-Doping Stabilized High-Performance P2–$Na_{0.66}Li_{0.18}Fe_{0.12}Mn_{0.7}O_2$ Cathode for Sodium Ion Batteries. *J. Am. Chem. Soc.* **2019**, *141*, 6680-6689.

(29) Cao, X.; Li, X.; Qiao, Y.; Jia, M.; Qiu, F.; He, Y.; He, P.; Zhou, H. Restraining Oxygen Loss and Suppressing Structural Distortion in a Newly Ti-Substituted Layered Oxide P2-$Na_{0.66}Li_{0.22}Ti_{0.15}$ $Mn_{0.63}O_2$. *ACS Energy Lett.* **2019**, *4*, 2409-2417.

(30) Okubo, M.; Yamada, A. Molecular Orbital Principles of Oxygen-Redox Battery

Electrodes. *ACS Appl. Mater. Inter.* **2017**, *9*, 36463-36472.

(31) Luo, K.; Roberts, M. R.; Hao, R.; Guerrini, N.; Pickup, D. M.; Liu, Y.; Edström, K.; Guo, J.; Chadwick, A. V.; Duda, L. C.; Bruce, P. G. Charge-Compensation in 3D-Transition-Metal-Oxide Intercalation Cathodes through the Generation of Localized Electron Holes On Oxygen. *Nat. Chem.* **2016**, *8*, 684-691.

(32) Hu, B.; Lou, X.; Li, C.; Geng, F.; Yang, M.; Shen, M.; Hu, B. Retarding Phase Transformation During Cycling in a Lithium- and Manganese-Rich Cathode Material by Optimizing Synthesis Conditions. *ChemElectroChem* **2019**, *6*, 1385-1392.

(33) Lin, T.; Schulli, T. U.; Hu, Y.; Zhu, X.; Gu, Q.; Luo, B.; Cowie, B.; Wang, L. Faster Activation and Slower Capacity/Voltage Fading: A Bifunctional Urea Treatment on Lithium-Rich Cathode Materials. *Adv. Funct. Mater.* **2020**, 1909192.

(34) House, R. A.; Maitra, U.; Jin, L.; Lozano, J. G.; Somerville, J. W.; Rees, N. H.; Naylor, A. J.; Duda, L. C.; Massel, F.; Chadwick, A. V.; Ramos, S.; Pickup, D. M.; McNally, D. E.; Lu, X.; Schmitt, T.; Roberts, M. R.; Bruce, P. G. What Triggers Oxygen Loss in Oxygen Redox Cathode Materials? *Chem. Mater.* **2019**, *31*, 3293-3300.

(35) Zhao, C.; Yao, Z.; Wang, J.; Lu, Y.; Bai, X.; Aspuru-Guzik, A.; Chen, L.; Hu, Y. Ti Substitution Facilitating Oxygen Oxidation in $Na_{2/3}Mg_{1/3}Ti_{1/6}Mn_{1/2}O_2$ Cathode. *Chem* **2019**, *5*, 2913-2925.

(36) Kim, S.; Aykol, M.; Hegde, V. I.; Lu, Z.; Kirklin, S.; Croy, J. R.; Thackeray, M. M.; Wolverton, C. Material Design of High-Capacity Li-rich Layered-Oxide Electrodes: Li_2MnO_3 and Beyond. *Energy Environ. Sci.* **2017**, *10*, 2201-2211.

(37) Hamaguchi, M.; Momida, H.; Oguchi, T. First-Principles Study on Cathode

Properties of Li_2MTiO_4 (M=V, Cr, Mn, Fe, Co, and Ni) with Oxygen Deficiency for Li-Ion Batteries. *J. Phys. Soc. Jpn.* **2018**, *87*, 044805.

(38) Nam, K.; Bak, S.; Hu, E.; Yu, X.; Zhou, Y.; Wang, X.; Wu, L.; Zhu, Y.; Chung, K.; Yang, X. Combining in Situ Synchrotron X-Ray Diffraction and Absorption Techniques with Transmission Electron Microscopy to Study the Origin of Thermal Instability in Overcharged Cathode Materials for Lithium-Ion Batteries. *Adv. Funct. Mater.* **2013**, *23*, 1047-1063.

(39) Xu, J.; Lee, D. H.; Clément, R. J.; Yu, X.; Leskes, M.; Pell, A. J.; Pintacuda, G.; Yang, X.; Grey, C. P.; Meng, Y. S. Identifying the Critical Role of Li Substitution in P2–$Na_x[Li_yNi_zMn_{1-Y-Z}]O_2$ (0<X, Y, Z< 1) Intercalation Cathode Materials for High-Energy Na-Ion Batteries. *Chem. Mater.* **2013**, *26*, 1260-1269.

(40) Zhang, K.; Kim, D.; Hu, Z.; Park, M.; Noh, G.; Yang, Y.; Zhang, J.; Lau, V. W.; Chou, S.; Cho, M.; Choi, S.; Kang, Y. Manganese Based Layered Oxides with Modulated Electronic and Thermodynamic Properties for Sodium Ion Batteries. *Nat. Commun.* **2019**, *10*.

(41) Wang, J.; Yang, M.; Zhao, C.; Hu, B.; Lou, X.; Geng, F.; Tong, W.; Hu, B.; Li, C. Unveiling the Benefits of Potassium Doping On the Structural Integrity of Li–Mn-rich Layered Oxides During Prolonged Cycling by Dual-Mode EPR Spectroscopy. *Phys. Chem. Chem. Phys.* **2019**, *21*, 24017-24025.

(42) Li, C.; Zhao, C.; Hu, B.; Tong, W.; Shen, M.; Hu, B. Unraveling the Critical Role of Ti Substitution in P2-$Na_xLi_yMn_{1-y}O_2$ Cathodes for Highly Reversible Oxygen Redox Chemistry. *Chem. Mater.* **2020**, *32*, 1054-1063.

(43) Zheng, X.; Li, P.; Zhu, H.; Rui, K.; Zhao, G.; Shu, J.; Xu, X.; Sun, W.; Dou, S. X. New Insights Into Understanding the Exceptional Electrochemical Performance of P2-type Manganese-Based Layered Oxide Cathode for Sodium Ion Batteries. *Energy Storage Mater.* **2018**, *15*, 257-265.

(44) Liu, Y.; Fang, X.; Zhang, A.; Shen, C.; Liu, Q.; Enaya, H. A.; Zhou, C. Layered P2-$Na_{2/3}[Ni_{1/3}Mn_{2/3}]O_2$ as High-Voltage Cathode for Sodium-Ion Batteries: The Capacity Decay Mechanism and Al_2O_3 Surface Modification. *Nano Energy* **2016**, *27*, 27-34.

(45) Wang, K.; Wan, H.; Yan, P.; Chen, X.; Fu, J.; Liu, Z.; Deng, H.; Gao, F.; Sui, M. Dopant Segregation Boosting High-Voltage Cyclability of Layered Cathode for Sodium Ion Batteries. *Adv. Mater.* **2019**, *31*, 1904816.

(46) Xu, G.; Amine, R.; Xu, Y.; Liu, J.; Gim, J.; Ma, T.; Ren, Y.; Sun, C.; Liu, Y.; Zhang, X.; Heald, S. M.; Solhy, A.; Saadoune, I.; Mattis, W. L.; Sun, S.; Chen, Z.; Amine, K. Insights Into the Structural Effects of Layered Cathode Materials for High Voltage Sodium-Ion Batteries. *Energy Environ. Sci.* **2017**, *10*, 1677-1693.

(47) Kim, H.; Ko, T.; Na, B.; Cho, W. I.; Chao, B. W. Electrochemical Properties of $LiM_xCo_{1-x}O_2$ [M = Mg, Zr] Prepared by Sol–Gel Process. *J. Power Sources* **2004**, *138*, 232-239.

(48) Ben Yahia, M.; Vergnet, J.; Saubanère, M.; Doublet, M. Unified Picture of Anionic Redox in Li/Na-ion Batteries. *Nat. Mater.* **2019**, *18*, 496-502.

(49) Assat, G.; Tarascon, J. Fundamental Understanding and Practical Challenges of Anionic Redox Activity in Li-ion Batteries. *Nat. Energy* **2018**, *3*, 373-386.

(50) Perez, A. J.; Jacquet, Q.; Batuk, D.; Iadecola, A.; Saubanère, M.; Rousse, G.; Larcher, D.; Vezin, H.; Doublet, M.; Tarascon, J. Approaching the Limits of Cationic and Anionic Electrochemical Activity with the Li-rich Layered Rocksalt Li_3IrO_4. *Nat. Energy* **2017**, *2*, 954-962.

(51) Li, C.; Geng, F.; Hu, B.; Hu, B. Anionic Redox in Na-based Layered Oxide Cathodes: A Review with Focus On Mechanism Studies. *Mater. Today Energy* **2020**, *17*, 100474.

Graphical Abstract